Research Square

Preprints are preliminary reports that have not undergone peer review.
They should not be considered conclusive, used to inform clinical practice,
or referenced by the media as validated information.

Twisted oxide lateral homostructures with conjunction tunability

Jan-Chi Yang (janchiyang@phys.ncku.edu.tw)
National Cheng Kung University https://orcid.org/0000-0002-3549-4392

Ping-Chun Wu
Department of Physics, National Cheng Kung University

Chia-Chun Wei
Department of Physics, National Cheng Kung University

Qilan Zhong
Key Laboratory of Polar Materials and Devices, Ministry of Education, Department of Electronic Engineering, East China Normal University

Sheng-Zhu Ho
National Cheng Kung University

Yu-You Chiu
National Cheng Kung University

Yi-De Liou
National Cheng Kung University

Chun-Chien Chiu
Department of Physics, National Cheng Kung University

Jo-Chi Hu
Department of Physics, National Cheng Kung University

Kei-Jie You
Department of Physics, National Cheng Kung University

Junding Zheng
Key Laboratory of Polar Materials and Devices, Ministry of Education, Department of Electronic Engineering, East China Normal University

Chun-Fu Chang
Max Planck Institute for Chemical Physics of Solids https://orcid.org/0000-0003-1803-2468

Rong Huang
East China Normal University

Chun-Gang Duan
East China Normal University

Yi-Chun Chen
National Cheng Kung University https://orcid.org/0000-0001-9435-8596

Chang-Yang Kuo

Department of Electrophysics, National Chiao Tung University

Physical Sciences - Article

Keywords: physics, epitaxial growth

Posted Date: May 17th, 2021

DOI: https://doi.org/10.21203/rs.3.rs-517146/v1

License: This work is licensed under a Creative Commons Attribution 4.0 International License.
Read Full License

Abstract

Epitaxial growth is of significant importance over the past decades, given it has been the key process of modern technology for delivering high-quality thin films. For conventional heteroepitaxy, the selection of proper single crystal substrates not only facilitates the integration of different materials but also fulfills interface and strain engineering upon a wide spectrum of functionalities. Nevertheless, the lattice structures, regularity and crystalline orientation are determined once a specific substrate is chosen. In this work, we reveal the growth of twisted oxide lateral homostructures with multiple conjunction degree of freedom. The twisted lateral homostructures with atomically sharp interfaces can be composed of epitaxial “blocks” with different crystalline orientations, ferroic orders and phases. We further demonstrate that this approach is universal for fabricating various complex systems. Our results establish an efficient pathway towards twisted lateral homostructures, allowing epitaxial films to be arbitrarily tailored at designated positions with unbounded in-plane conjunction tunability.

Introduction

Epitaxial growth, by which desired materials are deposited on crystalline substrates with well-aligned features, has been widely utilized to manufacture high-quality thin films with excellent functionalities, playing an indispensable role no matter from technological or scientific point of view. In conventional heteroepitaxy, the first consideration is the lattice mismatch between the desired materials and the single crystal substrates, in which the caused epitaxial strain in the grown thin films would lead to the modification of corresponding physical properties[1] and the formation of crystal defects[2]. Over the past decades, heteroepitaxy has been adopted to fabricate complex heterostructures, such as superlattices and vertically aligned arrays[3,4]. In these epitaxial systems, by taking advantages of complex interactions in different materials, novel phenomena/properties which can’t be obtained from individual parent materials are usually found[5,6]. Hitherto, heteroepitaxy is still a very broad and rapidly developing field, in which researchers are dedicated to comprehensive understanding and advanced modulation of novel phenomena/functionalities in epitaxial thin films, nanostructures and superlattices[7,8]. Nevertheless, the concept of conventional epitaxial growth is limited to vertical stacking, while the fabrication of lateral homostructures has yet been explored.

From traditional epitaxial growth point of view, the epitaxial thin films can only be grown along with relatively coherent lattices with respect to the chosen single crystal substrates and are confined to the similar crystal geometry. Additionally, despite the fact that the applied strain during epitaxial growth can be adopted to stabilize different phase polymorphs, yet it does not provide precise control upon the location and distribution of different phases and corresponding phase boundaries. For instance, coexisting tetragonal and rhombohedral phases of ferroelectric materials can be realized on a single substrate[9], on which the morphotropic phase boundary (MPB) exhibiting enhanced ferroelectricity can then be manipulated through an external electric field. However, the strain induced MPB can only be found at localized regions with microscale size and is usually randomly distributed[10,11]. Although the

precise control of lateral epitaxial structures has been a known task for next generation devices such as lateral p-n junctions[12,13] and gate-all-around transistors[14], the lack of efficient solutions has impeded the development of lateral junctions and related tunability. In light of above-mentioned considerations, herein, we reveal an original method assisted by inserting a freestanding layer with controllable twist angle to fulfill an efficient growth and the control of epitaxial lateral homostructures. With the combination of lithography and etching processes, the lateral homostructures can be fabricated at demanded positions with controllable conjunction angles. Besides, the same approach has been adopted to synthesize the lateral homostructures with distinct crystal orientations and polymorphs. In this work, taking $BiFeO_3$ (BFO) as a model system, with the insertion of a freestanding layer into the single crystal substrate, we demonstrate the growth of epitaxial homostructures with arbitrary conjunction angle tunability. Furthermore, distinct phases of BFO can be simultaneously “assembled” with atomically sharp phase boundary, which remarkably exhibits unconventional physical properties that are rarely seen in parent materials. The proposed approach paves a platform for the development of lateral homostructures with desired twisted angles, crystal orientations and phases conjunction degrees of freedom, thus opening up a distinct scene for epitaxial growth.

The process flow is illustrated in Fig. 1a. To begin with, an ultrathin $SrTiO_3$ (STO) thin film and a $(La,Sr)MnO_3$ (LSMO) sacrificial layer were grown on (110)-oriented STO single crystal substrate via pulsed laser deposition (see Methods). The STO/LSMO/STO heterostructure was then immersed in an acid solution, which was used to dissolve the LSMO layer, separating the grown STO thin film and STO substrate. The freestanding (110)-oriented STO layer (FS-STO) was then obtained and transferred onto the other (110)-oriented STO substrate. At the boundary of the covered and uncovered region, the [] directions of FS-STO and STO substrate form a natural but adjustable twisted angle (denoted as *phi*), as shown in Fig. 1a. A (110)-oriented STO twisted template with misaligned in-plane crystalline directions is therefore derived. Herein, a classic room-temperature magnetoelectric multiferroic material with coupled ferroelectricity and antiferromagnetism, BFO, was chosen as a model system for exploring the conjunction tunability. When it comes to epitaxial growth of BFO, the topography and ferroelectric domain patterns are determined by constrains and orientation applied by the substrate beneath. The special stripe feature in epitaxial (110)-oriented BFO is therefore a direct visual evidence once the crystalline directions are altered. Fig. 1b shows the topographic images of BFO grown on pristine STO region (BFO_{AG}), near the boundary and on FS-STO (BFO_{FS}), respectively. Given that the topography stripes in (110)-oriented BFO are always aligned with the [001] direction of STO[15], the twisted feature of the grown BFO at the boundary can be clearly observed. Please be noted that the twisted feature of the epitaxial (110)-oriented BFO can also be resolved by X-ray diffraction phi-scan, as shown in Extended Data Fig. 1. Noticeably, the BFO grown on top of the twisted template follows the underlying crystalline patterns of the FS-STO layer and the STO substrate, respectively, forming a twisted lateral homostructure/homojunction. This suggests that the grown epitaxial BFO films tend to follow crystalline architectures of the freestanding layer and single crystal substrate right beneath. Our result is different from remote epitaxy through graphene layer, where the potential filed from the single crystal substrate cannot be completely screened[16,17]. Instead, the thickness of the chosen FS-STO layer is sufficient to

screen the potential filed for the substrate, thus the grown BFO would follow the crystalline pattern of the underlying twisted template. This result is also in good agreement with our density-functional theory (DFT) calculations (see Supplementary Information Note S1).

To reveal detailed structure of the lateral homostructures grown on the twisted template, the microstructure of a well-defined 90^o twisted BFO homostructure is studied via transmission electron microscopy (TEM). A typical low magnification cross-sectional bright-field TEM image along the STO[001] direction (Fig. 2a) shows the clear boundaries at the STO/BFO_{FS}/BFO_{AG} interface. Moreover, the high-resolution transmission electron microscopy (HRTEM) images viewed along the STO [001] zone axis (Fig. 2b) and STO [] zone axis (Fig. 2c), respectively, show the detailed structure of the interface region. It can be clearly seen that the BFO_{AG} was epitaxially grown on the STO substrate with flat and sharp interface as marked with a yellow line. Whereas the BFO_{FS} was epitaxially grown on a brighter ~5 nm STO_{FS} layer as marked with two green lines. The twisted BFO_{AG}/BFO_{FS} interface is also very sharp as marked with a yellow dashed line. The corresponding selected area electron diffraction (SAED) patterns of the STO substrate, BFO_{AG} and BFO_{FS} are shown in Fig. 2d, e, f, respectively. The epitaxial relationship of STO (110)//BFO_{AG} (110)//BFO_{FS} (110) and STO [001]//BFO_{AG} [001]//BFO_{FS} [] is revealed. The SAED and HRTEM results unanimously manifest the high quality of the 90^o twisted BFO homostructure. The orthogonal stripes of (110)-oriented BFO at the boundary revealed by atomic force microscopy (AFM) further validate the relationship observed by the micro-structural characterization (see Supplementary Information Note S2). It is remarkable that the twisted phi angle of the homostructures can be arbitrarily controlled through the alignment process during transfer, as shown in Supplementary Information Fig. S2.

Furthermore, to understand the atomic arrangement at the boundary of BFO_{AG} region and BFO_{FS} region, the high-angle annular dark-field (HAADF) observations were carried out in a spherical aberration corrected scanning TEM (Cs-corrected STEM) for the samples of Fig. 2b, c, as shown in Fig. 2g, h, respectively. When viewed along the STO [001] direction, the BFO_{AG} also aligned to the [001] zone axis, showing typical perovskite structure in the upper-right of Fig. 2g. The BFO_{AG} (010) plane is about 45^o with the STO substrate surface and clear facets of the BFO_{AG} (010) plane at the BFO_{AG}/BFO_{FS} interface can be seen, as indicated with a yellow dashed line. However, when observed along the STO [] zone axis (Fig. 2h), which is perpendicular to the STO [001] zone axis, the BFO_{AG}/BFO_{FS} interface became nearly perpendicular to the STO substrate surface though the BFO_{FS}(010) plane appears in the left side of Fig. 2h. This indicates that the facets of FS-STO and BFO_{AG} (001) planes governed the conjunction geometry of the BFO_{AG}/BFO_{FS} interface, as marked with the yellow dashed lines in Fig. 2g, h. To further explore the electronic state near the interface, an electron energy-loss spectroscopy (EELS) line-scan along the direction perpendicular to the BFO_{AG} / BFO_{FS} interface in Fig. 2h was carried out. The O-*K* edge (Fig. 2i) near the interface (point 3 and 4) clearly show that the peak *a* is decreased, compared with that from the interior (point 1 and 6), indicating the existence of oxygen vacancy at the interface region[18] Correspondingly, the Fe-L_3 edge at the interface region show slightly chemical shift to the lower energy

side, as indicated by the red arrows in Fig. 2j, suggesting that the valence state of Fe decreased slightly at the interface[19]. To affirm the high quality BFO homojunction without detectable interdiffusion, atomic resolved X-ray energy dispersive spectroscopy (EDS) mapping of interface was also performed, as shown in Extended Data Fig. 2.

Utilizing the ability to combine different crystallographic orientations in the in-plane, a device prototype composed of BFO blocks with designated ferroelectric polarizations and antiferromagnetic directions is demonstrated, as schematically illustrated in Fig. 3a. Firstly, FS-STO (110) was transferred onto STO (110) substrate, forming an in-plane twisted angle of 90^{o} with respect to their individual [001] directions. Through a combination of photolithography and etching processes (see Methods), the FS-STO was then etched into well-defined patterns. Last, as above-mentioned, BFO thin film was grown on the patterned twisted template. Following similar flows, any patterned lateral homostructures with relative in-plane twisted angle can be fabricated. As shown in Fig. 3b, the topographic image reveals the vertical stripes embedded in the horizontal stripe matrix, verifying the feasibility of arbitrary control of lateral conjunctions. Besides, vector-piezo-force microscopy (vector-PFM) analysis with respect to different cantilever orientation was carried out to identify the ferroelectric domain patterns of the cellular structure. As shown in Fig. 3c, the PFM image was taken with cantilever pointing along [] direction of pristine STO substrate. For patterned squares inside the matrix, a single domain feature with net ferroelectric polarization perpendicular to the cantilever is observed, while the net ferroelectric polarization of the matrix is parallel to the cantilever. The perpendicular polarization configuration could also be identified by rotating the probing cantilever 45˚ counterclockwise, as shown in Fig. 3d.

In multiferroic BFO, the relationship between the spontaneous polarization and antiferromagnetism is subject to epitaxial constrains[20,21]. With the development of twisted lateral homostructures, the arrangement of ferroic orders can be controlled in a more flexible and innovative manner. To investigate the antiferromagnetic characteristics of the patterned BFO (110) lateral device, we performed X-ray linear absorption spectroscopy (XLAS) measurements on the Fe $L_{2,3}$-edge of the BFO_{AG} and BFO_{FS} thin film with a linear polarization vector (**E**) paralleled to the pristine STO $[001]_{SUB}$. Fig. 3e shows the XLAS mapping of intensity ratio I_B/I_A, where I_B and I_A are the XLAS intensity taken at Fe L_2-edge around the characteristic energy denoted as A and B, respectively, as indicated in Fig. 3f. The size and the arrangement of the patterned squares are consistent with the PFM results and our designer pattern. The Fe L_2-edge XLAS spectra taken from BFO_{AG} film and BFO_{FS} are shown in Fig. 3f, in which a clear dichroism correlated to the relative orientation of polarization vector **E**, crystallography-axis, and the antiferromagnetic axis[21-26] can be observed. To further extract the information provided from the dichroism, we performed configuration interactions cluster calculations. It is a theoretical approach that takes into account the full-multiplet Coulomb interaction, local crystal field, local spin-orbital coupling, local spin direction, and hybridizations with ligand atoms[27-29], and a well-proven tool that can be adopted to effectively simulate the X-ray absorption spectra. In Extended Data Fig. 3, we show the calculated XLAS of both BFO_{AG} to BFO_{FS} regions with **E**//STO $[001]_{SUB}$ based on two different scenarios: (i) antiferromagnetic-axis rotated by 90 degrees, and (ii) both antiferromagnetic-axis and crystallography-

axis rotated by 90 degrees. By comparing the experimental and simulated results, two nearly identical dichroism spectra can be obtained when scenario (ii) is adopted. Namely, our simulation indicates that the antiferromagnetic- and crystallography-axes of BFO grown on pristine STO and FS-STO regions exhibit a perpendicular feature, as depicted in Fig. 3f. The controllable arrangement of both ferroelectricity and antiferromagnetic-axes using BFO validates the feasibility to design lateral crystalline orientation/domain patterns and related homostructures with conjunction twisted angle tunability.

The transition region and interfaces in strongly correlated oxides, for example, domain walls and phase boundaries, always exhibit unconventional physical phenomena and enhanced functionalities, such as low dimensional interfacial conduction, superconductivity, enhanced magnetism and so on[8,30,31]. Here, we further demonstrate the versatility of constructing lateral homostructures composed of the polymorphs with different crystalline symmetry via the insertion of epitaxial freestanding layers. To do so, freestanding (001)-oriented STO layer was transferred onto $LaAlO_3$ (LAO) substrate with ~50% coverage to create a template offering two different lattice mismatches. After deposition, BFO grown on FS-STO exhibits rhombohedral-like phase (R-BFO), while the BFO grown on LAO possesses tetragonal-like phase (T-BFO), as illustrated in Fig. 4a. From the AFM images shown in Fig. 4b, a phase boundary separating two different crystallography of BFO was artificially created. It is worth mentioning that the coexisted yet randomly-distributed T-R phase boundary of BFO can be found in a strain-driven morphotropic mixed-phase system, where the BFO thin films are grown on LAO substrate[9]. As shown the morphology image in Fig. 4b, a steep and clear boundary between R-BFO and T-BFO can be identified, resulting in a step height ~5 nm, which is consistent with the thickness of FS-STO. The structures of BFO on freestanding STO layer and LAO substrate was revealed by X-ray diffraction, as shown in the RSM around LAO (001) peaks in Fig. 4b where the feature peaks of T-BFO, R-BFO, STO and LAO are labeled correspondingly. Further RSM images near LAO (103) and STO (103) indicate that T-BFO and R-BFO are subject to the epitaxial strain applied by LAO substrate and FS-STO, respectively. Detailed structural properties related to the symmetries of BFO polymorphs, FS-STO and LAO substrate can be found in Extended Data Fig. 4.

To probe the local transport behavior near the homojunction/boundary between R-BFO and T-BFO, conductive atomic force microscopy (C-AFM) was employed, which simultaneously mapped the surface morphology and corresponding conductivity. The corresponding C-AFM image taken with applied tip bias of 1.6 V shown in Fig. 4c indicates an obvious enhanced electrical conduction at the T-R phase boundary compared to the individual R-BFO and T-BFO region. The unconventional conduction was further examined by the I-V curve at phase boundary, which shows a nonlinear Schottky diode-like characteristic with small hysteresis. In such a system, there are several mechanisms that might dominate the potential factors for the modification of electronic structures at the artificially-created phase boundary, leading to the enhanced conductivity. First, the ferroelectric and structural discontinuity at the interface is correlated to the local distortion and band-alignment of the homostructure, which might affect the charge accumulation and the electronic band structure across the interface[32,33]. Second, the modification of chemical bonds at the semi-coherent interfaces accompanies the reconstruction of the defect level at the interface. Third, the changes in Fe–O–Fe bond angle and unusual oxygen octahedral rotation at the

interface could affect the orbital overlapping and thus varying the bandgap at phase boundary[34,35]. To this end, the modification of local band structure as well as the accumulation of the charged defects at the phase boundary all contribute to the enhanced conductivity at the artificial R-BFO and T-BFO interface.

Through the insertion of the extremely thin freestanding layers, we are able to synthesize twisted lateral homostructures with orientation and phase conjunction turnabilities. Additionally, the twisted conjunction with different out-of-plane lattice orientations is also feasible (please refer to Supplementary Information Note S3). To verify such an approach is universal for manufacturing different complex systems, twisted lateral homostructures composed of a classic high-temperature superconductor, $YBa_2Cu_3O_{7-x}$ (YBCO), were also demonstrated, as presented in Extended Data Fig. 5. The controllable twisted angle at the boundary of the same materials offers a unique platform in developing emergent phenomena. Such an approach is compatible with modern photolithography processes, with which we have successfully revealed the patterned lateral homostructures with artificially designable ferroic orders and orbital configurations. By transferring freestanding thin film onto the substrate with dissimilar lattice structure, we further show that distinct phases of the same material can be simultaneously assembled, forming a sharp interface exhibiting distinct physical properties. Our results lay a groundwork for the design of twisted lateral homostructures, which might contribute to advanced manipulation of strongly correlated phenomena in complex systems through artificially modified electronic structure and crystal geometry.

Methods

Synthesis of the lateral homostructures.

The samples were fabricated by pulsed laser deposition (PLD), using KrF (248 nm) excimer laser. The $SrTiO_3$ (STO) thin films were deposited on (La,Sr)MnO_3 (LSMO) buffered (110)-oriented STO substrates. The STO was deposited at oxygen pressure of 100 mTorr at 700 °C with a laser power of 250 mJ and laser repetition rate of 10Hz, while the LSMO were deposited at oxygen pressure of 100 mTorr at 750 °C with a laser power of 250 mJ and laser repetition rate of 10 Hz. Thereafter, the heterostructure was immersed in hydrochloric acid to dissolve LSMO buffered layer and to separate STO film from single crystal substrate. The freestanding STO was then transferred onto another (110)-oriented STO single crystal substrate, having a twisted angle with respect to the STO single crystal substrate. Last, the $BiFeO_3$ thin film was deposited at oxygen pressure of 85 mTorr at 680 °C with a laser power of 250 mJ and laser repetition rate of 10 Hz.

Structural analysis.

The crystal structure of the as-grown thin films and homostructures was characterized by synchrotron-based X-ray high-resolution 8 circle diffractometer with beam energy of 10 keV and size of 0.30.7 mm^2 at beamline 17B and 13A1 in the National Synchrotron Radiation Research Center, Taiwan.

Transmission electron microscopy.

Cross-sectional TEM specimens were prepared by focused ion beam (FIB, Helios G4UX, FEI, America). In order to reduce the damage, a high vacuum film plating instrument was first used to evenly coat a layer of C film ~50 nm thick on the surface of the film. HRTEM observations were carried out using a field emission microscope (JEM-2100F, JEOL, Japan) at an acceleration voltage of 200 kV. Further STEM-HAADF imaging were performed with an Cs-corrected STEM operating at 300 kV (Grand ARM-300, JEOL, Japan) equipping X-ray energy dispersive spectrometer (JED-2300T) and a K2 camera. In EELS analysis, an entrance aperture of 2.5 mm was used and the energy resolution of 1.03 eV was determined by measuring the full-width half-maximum (FWHM) of the zero-loss peak with the energy dispersion of 0.25eV/channel. The EELS spectra were recorded with spectrum image mode to increase the signal/noise ratio, and the acquisition time was about 0.2s per pixel (total acquisition time is about 3 minutes).

Lateral homostructure devices.

The lateral homostructure devices were fabricated by a combination of photolithography and etching processes. First, freestanding STO (110) thin film was transferred onto (110)-oriented STO substrate with 90 degrees twist angle. Later, photoresist with geometric patterns were created on the twist FS-STO/STO template via the photolithography method. The patterns were then covered by 200 nm chromium, deposited by an e-beam evaporator, as a protective layer. After the removal of photoresist, the revealed FS-STO (squares) were further etched by the reactive ion etching (RIE). During the etching process, the chamber was kept at 100 mTorr with a methane flow of 50 sccm and the plasma power generator was controlled at 500 mW where the etching rate is 0.4 nm/min. The well-defined pattern of FS-STO/STO can then be obtained after the removal of the chromium layer by CR-7 chromium etchant. Thereafter, BFO was grown on the patterned FS-STO/STO template using PLD.

X-ray absorption spectroscopy.

The X-ray absorption spectroscopy measurements were conducted at TPS-45 beamline, National Synchrotron Radiation Research Center (NSRRC). The beam resolution was set to be around 50 meV with the spot size around 3*3um.

Configuration interactions cluster calculations

The calculation was processed using Quanty[36-39], a script language which allows the user to program and resolve many bodies quantum mechanical problems in second quantization. Quanty based configuration interactions cluster calculations is then utilized to simulate $L_{2,3}$-edge X-ray absorption spectra of the 3*d*-transition metal oxides[36].

Atomic force microscopy and piezo-force microscopy.

The SPM based studies (atomic force microscopy and piezo-force microscopy) for topography and PFM were operated via the “closed loop” commercial scanning probe microscope system (Dimension Icon,

Bruker) with software Nanoscope 9.14 in scanasyst mode and vertical-optimized PFM mode, respectively. All PFM images were recorded in the matrix of 256 x 256 with an a.c. voltage of 2 V and 7 kHz applied on the Pt/Ir-coating conductive probe (elastic force constant ~7.4 N m^{-1}). The in-plane PFM images of BFO homostructures with different twisted angles were obtained using a lock-in amplifier (SR-830, Stanford Research Systems).

Declarations

Data availability

The authors declare that the data supporting the findings of this study are available within the main and supplemental figures. All data is available in the Source Data File. Source data are provided with this paper.

Acknowledgements

This work is supported by the Ministry of Science and Technology (MOST) in Taiwan under grant no. MOST 109-2636-M-006-003 (Young Scholar Fellowship Program) and 108-2112-M-006-018 -MY3. R.H. is supported by the National Key Research and Development Program of China (2017YFA0303403) and the National Natural Science Foundation of China (Grant No. 61974042). C.-Y.K. acknowledges support from the Max-POSTECH/Hsinchu Center for Complex Phase Materials. The authors also thank MSSORPS Co., Ltd. for high-quality TEM sample preparation and preliminary observation of HRTEM. The research is also supported in part by Higher Education Sprout Project, Ministry of Education to the Headquarters of University Advancement at National Cheng Kung University (NCKU). The authors thank Prof. Y. H. Chu for his insightful suggestions and inputs in this work.

Author contributions

P.-C.W., Y.-C.L. J.-C.H. K.-J.U. and C.-C.W. processed the sample growth and X-ray diffraction analysis. S.-Z.H., Y.-D.L., and Y.-C.C. conducted characterizations of scanning probe microscopy, and analyzed the data. Q.Z. and R.H. carried out transmission electron microscopy characterization and processed high-angle annular dark-field imaging and resolved the crystal structure. J.Z and C.-G.D. conducted the first-principle calculations. C.-C.C., C.-F.C. and C.-Y.K processed X-ray absorption based measurements and analyzed the data. J.-C.Y. led the project, conceived main idea, and co-wrote the manuscript draft with P.-C.W..All authors contributed to the manuscript. P.-C.W., C.-C.W. and Q.Z. contributed equally in this work.

Competing interests

The authors declare no competing interests.

Additional information

Supplementary information The online version contains supplementary material available.

Correspondence and requests for materials should be addressed to J. C. Yang.

Peer review information

Reprints and permissions information is available at www.nature.com/reprints.

References

1. Schlom, D. G. et al. Strain tuning of ferroelectric thin films. *Rev. Mater. Res.* **37**, 589-626 (2007).
2. Freund, LB. & Suresh, S. Thin Film Materials: Stress, Defect Formation and Surface Evolution. *Cambridge, UK: Cambridge Univ. Press.* 768 pp. (2003).
3. Koster, G., Huijben, M. & Rijnders, G. Metal Oxide-Based Thin Film Structures. *Elsevier, Inc.*27– 52 (2018)
4. MacManus-Driscoll, J. L. Self-assembled heteroepitaxial oxide nanocomposite thin film structures: designing interface-induced functionality in electronic materials. *Funct. Mater.* **20**, 2035-2045 (2010).
5. Zavalinche, F. et al. Electric field-induced magnetization switching in epitaxial columner nanostructures. *Nano Lett.* **5**, 1793-1796 (2005).
6. Ramesh, R. & Spaldin, N. A. Multiferroics: progress and prospects in thin films. *Mater.* **6**, 21-29 (2007).
7. Mannhart, J. & Schlom, D. G. Oxide interfaces-an opportunity for electronics. *Science* **327**, pp. 1607-1611 (2010).
8. Zubko, P., Gariglio, S., Gabay, M., Ghosez, P. & Triscone, J. M. Interface physics in complex oxide heterostructures. *Rev. Condens. Matter Phys.* **2**, 141-165 (2011).
9. Zeches, R. J. A strain-driven morphotropic phase boundary in $BiFeO_3$. *Science* **326**, pp. 977-987 (2009).
10. Maran, R. et al. Interface control of a morphotropic phase boundary in epitaxial samarium modified bismuth ferrite superlattices. *Rev. B* **90**, 245131 (2014).
11. Han M. J. et al. Coexistence of rhombohedral and orthorhombic phases in ultrathin $BiFeO_3$ films driven by interfacial oxygen octahedral coupling. *Acta Materilia* **145**, 220-226 (2018).
12. Duan, X. et al. Lateral epitaxial growth of two-dimensional layered semiconductor heterojunctions. *Nanotechnol.* **9**, 1024-1030 (2014).
13. Li, M. Y. et al. Epitaxial growth of a monolayer WSe_2-MoS_2 lateral p-n junction with an atomically sharp interface. *Science* **349**, pp. 524-528 (2015).
14. Veloso, A., De Keersgieter, A., Matagne, P., Horiguchi, N. & Collaert, N. Advances on doping strategies for triple-gate finFETs and lateral gate-all-around nanowire FETs and their impact on device performance. *Sci. Semicond. Process.* **6**, 2-12 (2017).
15. Sharma, Y. et al. Long-range stripe nanodomains in epitaxial (110) $BiFeO_3$ thin films on (100) $NdGaO_3$ *Sci. Rep.* **7**, 4857 (2017).

16. Kim, Y. et al. Remote epitaxy through graphene enables tow-dimensional material-based layer transfer. *Nature* **544**, 340-343 (2017).
17. Bae, S. H. et al. Graphene-assisted spontaneous relaxation towards dislocation-free heteroepitaxy. *Nanotechnol.* **15**, 272-276 (2020).
18. Kim, Y. H., Bhatnager, A., Pippel, E., Alexe, M. & Hesse, D. Microstructure of highly strained $BiFeO_3$ thin films: Transmission electron microscopy and eletron-energy loss spectroscopy studies. *Appl. Phys.* **115**, 043526 (2014).
19. Kim, Y. M. et al. Direct observation of ferroelectric field effect and vacancy-controlled screening at the $BiFeO_3/La_xSr_{1-x}MnO_3$ *Nat. Mater.* **13**, 1019-1025 (2014).
20. Jang, H. W. et al. Strain-induced polarization rotation in epitaxial (001) $BiFeO_3$ thin films. *Rev. Lett.* **101**, 107602 (2008).
21. Chen, Z. et al. Complex strain evolution of polar and magnetic order in multiferroic $BiFeO_3$ thin films. *Commun.* **9**, 3764 (2018).
22. Kuiper, P., Searle, B. G., Rudolf, P., Tjeng, L. H. & Chen, C. T. X-ray magnetic dichroism of antiferromagnet Fe_2O_3: the orientation of magnetic moments observed by Fe 2p X-ray absorption spectroscopy. *Rev. Lett.* **70**, 1549 (1993).
23. Arenholz, E., van derLaan, G., Chopdekar, R. & Suzuki, Y. Anisotropic x-ray magnetic linear dishcroism at the Fe $L_{2,3}$ edges in Fe_3O_4. *Rev. B.* **74**, 094407 (2006).
24. Kuo, C. Y. et al. Single-domian multiferroic $BiFeO_3$ *Nat. Commun.* **7**, 12712 (2016).
25. Liou, Y. D. et al. Extremely fast optical and nonvolatile control of mixed-phase multiferroic $BiFeO_3$ via instantaneous strain perturbation. *Adv Mater.*
26. Yang, J. C. et al. Electrically enhanced magnetization in highly strained $BiFeO_3$ *NPG Aisa Mater.* **8**, e269 (2016).
27. DeGroot, F. M. X-ray absorption and dichroism of transition metals and their compounds. *Electron. Spectros. Relat. Phenomena* **67**, 529 (1994).
28. Tanaka, A. & Jo, T. Resonant 3d, 3p and 3s photoemission in transition metal oxides predicted at 2p threshold. *Phys. Soc. Jpn.* **63**, 2788-2807 (1994).
29. Bocquet, A. E. et al. Electronic structure of early 3d-transition-metal oxides by analysis of the 2p core-level photoemission spectra. *Rev. B*. **53**, 1611-1170 (1996).
30. Catalan, G., Seidel, J., Ramesh, R. & Scott, J. F. Domain wall nanoelectronics. *Mod. Phys.* **84**, 119 (2012).
31. Hwang, H. Y. et al. Emergent phenomena at oxide interfaces. *Mater.* **11**, 103-113 (2012).
32. Kim, K. E. et al. Electric control of straight stripe conductive mixed-phase nanostructures in La-doped $BiFeO_3$. *NPG Asia Mater.* **6**, e81 (2014).
33. Heo, Y. et al. Enhanced conductivity at orthorhombic-rhombohedral phase boundaries in $BiFeO_3$ thin film. *NPG Asia Mater.* **8**, e297 (2016).

34. Qi, T., Grinberg, I. & Rappe, A. M. Band-gap engineering via local environment in complex oxides. *Rev. B* **83**, 224108 (2011).
35. Catalan, G. On the link beween octahedral rotations and conductivity in the domain walls of $BiFeO_3$. *Ferroelectrics* **433**, 65-73 (2012).
36. Haverkort, M. W., Zwierzycki, M. & Andersen, O. K. Multiplet ligand-field theory using Wannier orbitals. *Rev. B* **85**, 165113 (2012).
37. Lu, Y., Hoppner, M., Gunnarsson, O. & Haverkort, M. W. Efficient real-frequency solver for dynamical mean-field theory. *Rev. B* **90**, 085102 (2014).
38. Haverkort, M. W. et al. Bands, resonances, edge singularities and excitions in core level spectroscopy investigated within the dynamical mean-field theory. *Phys. Lett.* **108**, 57004 (2014).
39. Haverkort, M. W. Quanty for core level spectroscopy-excitons, resonances and band excitations in time and frequency domain. *Phys.: Conf. Sereis* **712**, 012001 (2016).

Figures

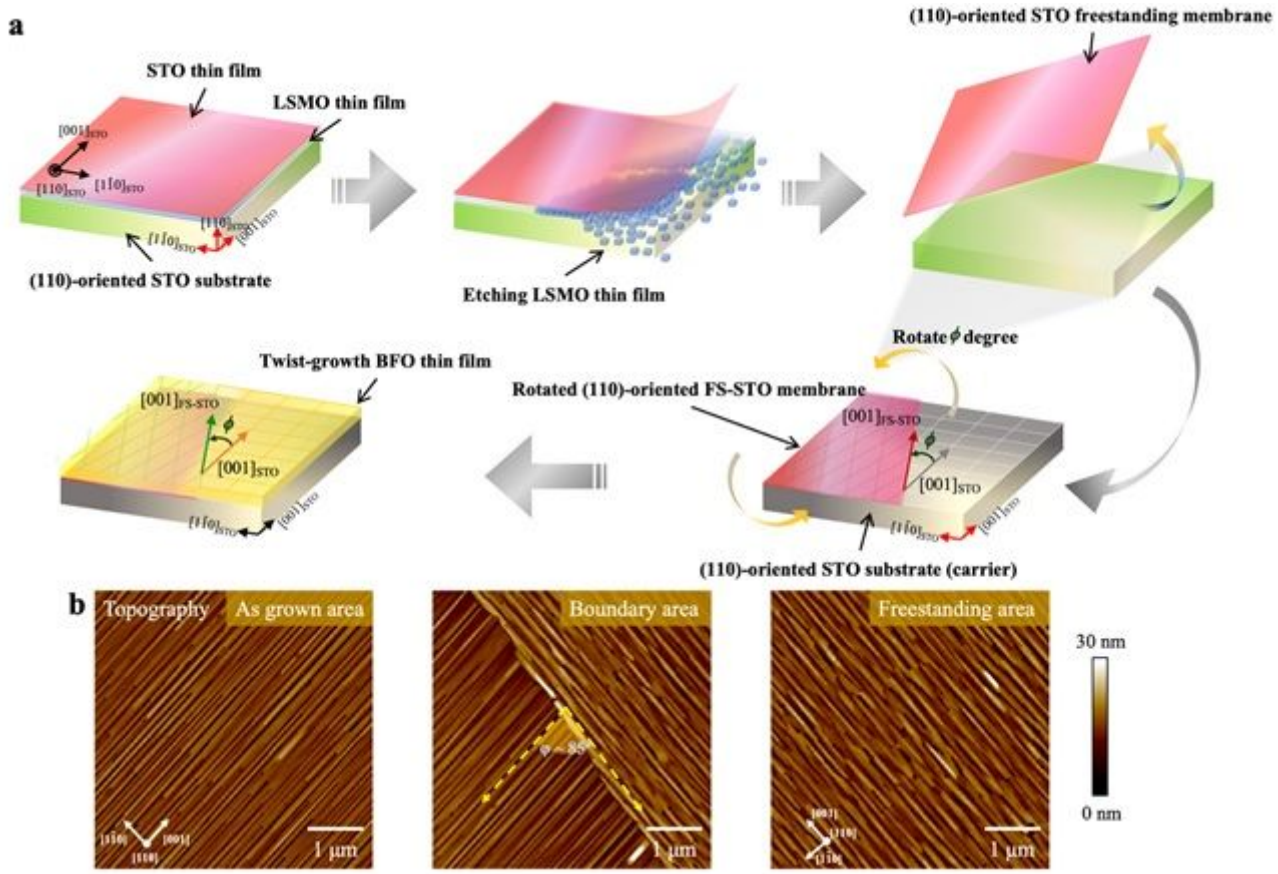

Figure 1

Synthesis of the lateral oxide homostructures. a Schematic illustration of lateral oxide homostructures. (1) Growth of SrTiO3 (STO) with a (La,Sr)MnO3 (LSMO) sacrificial layer on (110)-oriented STO single crystal substrate. (2) Etching of the LSMO sacrificial layer. (3)(4) Releasing and transferring the

freestanding STO layer with designated twisted angle with respect to the selected single crystal substrates. (5) Deposition of functional oxide film (BiFeO3, BFO) on the twisted template. b Topography images of (110)-oriented BFO grown on pristine STO, border, and FS-STO region, respectively. The [001]pc-oriented stripes serve as the direction reference of epitaxial BFO, identifying the in-plane directions of (110)-oriented BFO and the twisted angle (denoted as angle phi) at the boundary of pristine STO and FS-STO region.

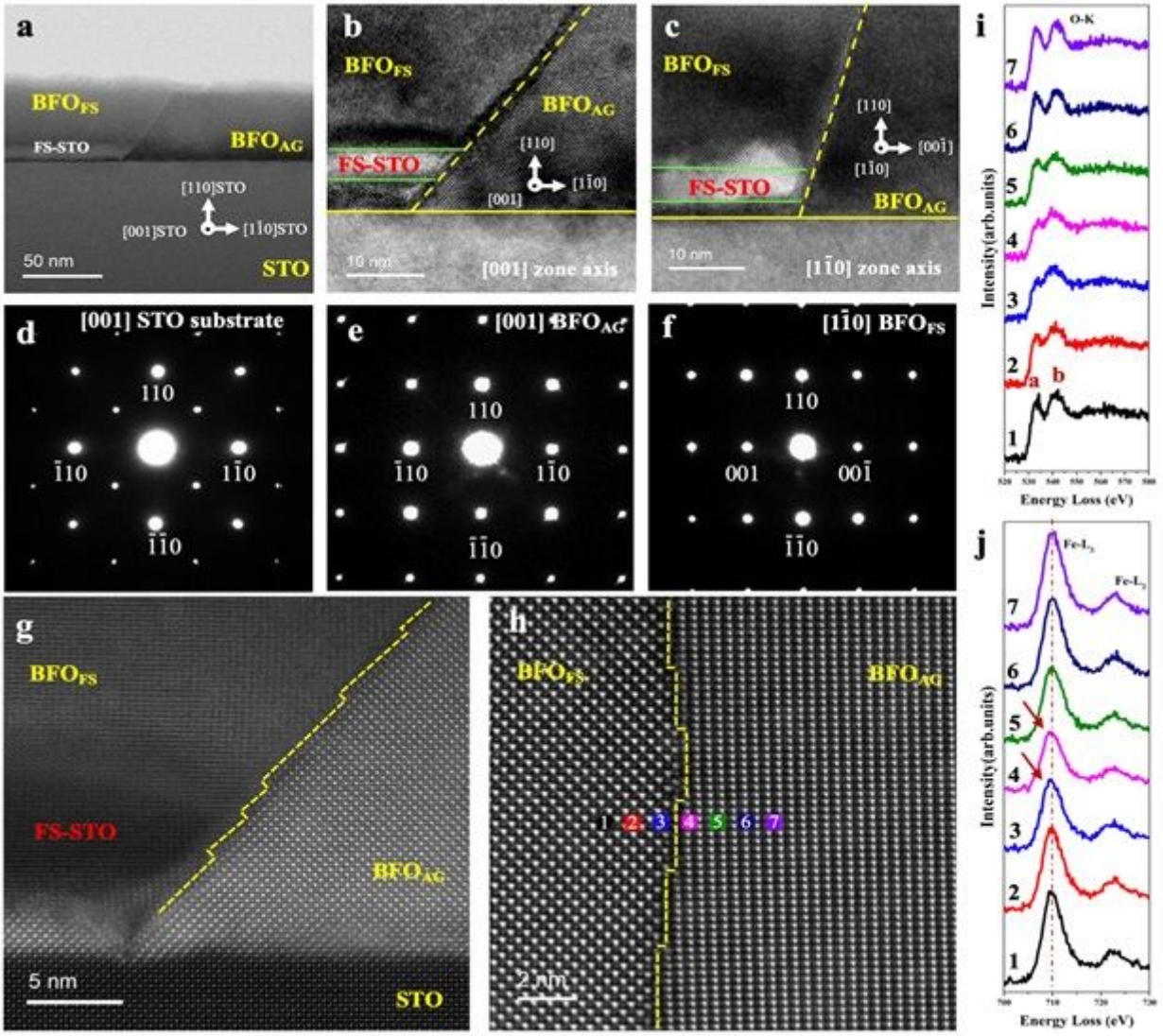

Figure 2

Microstructure characterization of the BFO lateral homostructure. a Typical cross-sectional TEM image taking along [001] direction of STO substrate. b and c HRTEM images of the interface area along the [001] and [11¯0] direction of STO substrate, respectively. d, e and f SAED patterns of pristine STO, BFOAG and BFOFS, respectively, corresponding to figure A. g HAADF image of the interface area corresponding to figure B. A gap between FS-STO and STO can be clearly observed, where the space was further filled with BFO. h HAADF image of the BFOFS/BFOAG interface from figure C. i and j O-K and Fe-L2,3 edge of BFO acquired along the line perpendicular to the interface in figure H.

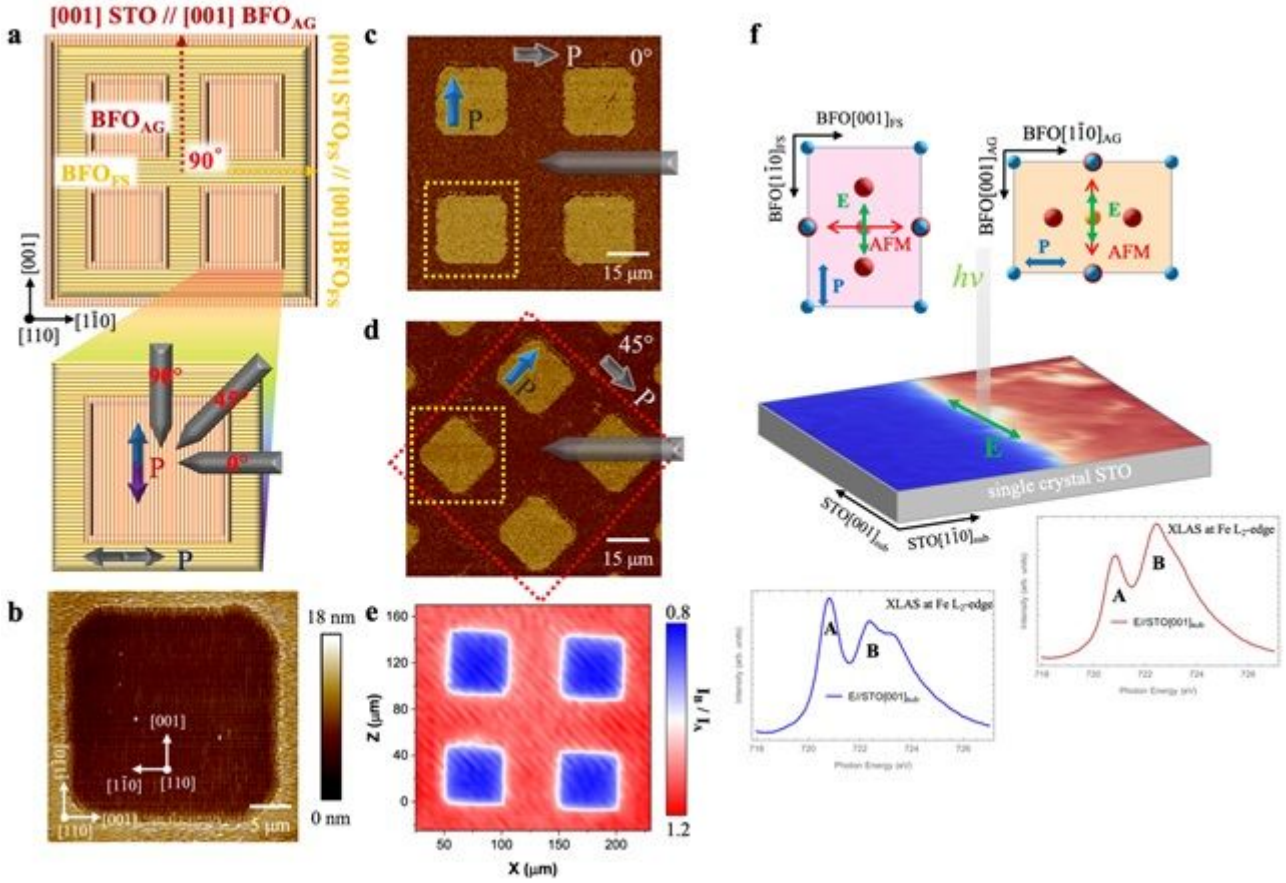

Figure 3

Design of patterned lateral homostructures. a Schematic of the designer BFO (110) lateral homostructures, in which the stripes along BFO [001] direction are designed to be orthogonal. The enlarged area shows the direction of the AFM cantilever. b Topography image of the patterned lateral (110)-oriented BFO homostructures. The orthogonal stripes of BFO verify the feasibility of the designer patterns. c and d In-plane phase of the lateral BFO (110) homostructures with the probing cantilever parallel and 45o to [001] direction of FS-STO. The net polarizations of BFOAG and BFOFS are shown in blue and gray arrows, respectively. e IB/IA ratio of XLAS mapping on the patterned lateral homostructures. f IB/IA ratio of XLAS mapping across the boundary of BFOAG and BFOFS area. The XLAS Fe L2-edge spectra taken from the as-grown BFO film and the BFO film on FS-STO are presented in blue and red colors, respectively (lower panels). The upper panels schematically show the correlation of the ferroelectric polarization and antiferromagnetic axes of the patterned homostructures.

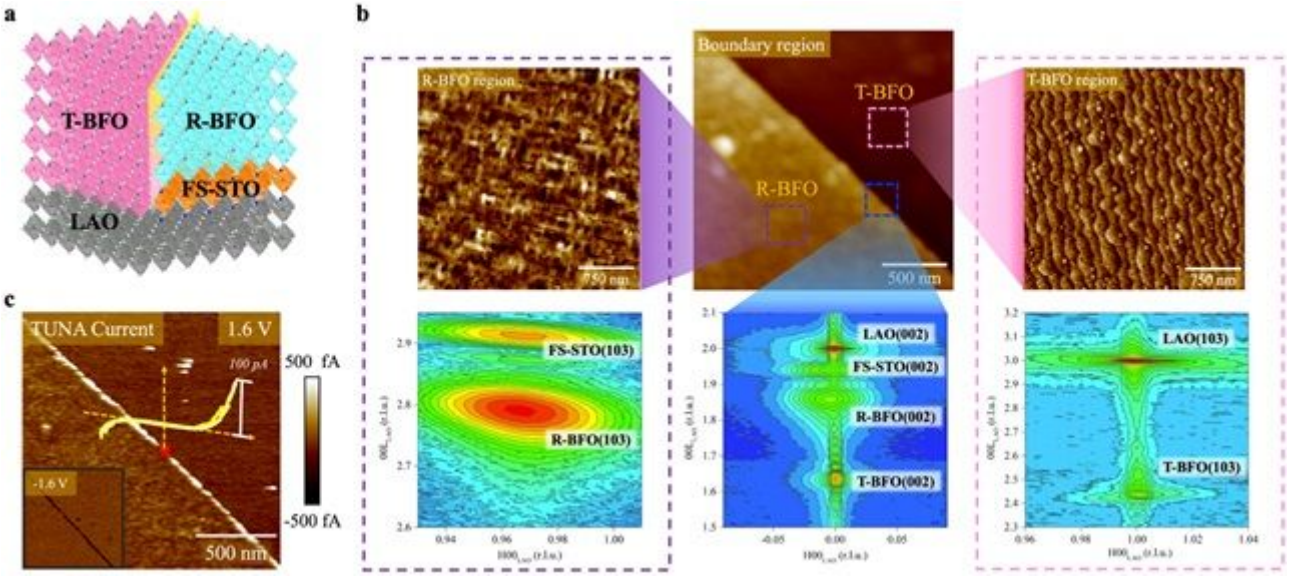

Figure 4

Artificial creation of BFO polymorph phase boundary. a The designer lateral homostructure composed of coexisted tetragonal-like and rhombohedral-like BFO phases. Freestanding STO layer (orange layer) was transferred onto LAO substrate (grey substrate), forming a twisted template with distinct lattice constrains on both sides. The pink and blue lattices represent the tetragonal-like (T-BFO) and rhombohedral-like (R-BFO) BFO phases, respectively. b Topography image near the boundary of rhombohedral-like and tetragonal-like BFO. Corresponding RSM images around LAO (003), FS-STO (103), LAO (103) are shown in the lower panel, respectively. Four characteristic peaks can be identified around LAO (003) as LAO (003), FS-STO (003), R-BFO (003) and T-BFO (003), respectively, as labeled in the images. RSM image around LAO (103) indicates the T-BFO forms on LAO substrate and RSM around STO (103) evidences that the R-BFO forms on the FS-STO layer. c Conductive AFM image taken at the phase boundary with a tip bias of 1.6 V, where the right-bottom inset shows the conductive AFM image taken at tip bias of -1.6 V. The I-V curve and corresponding current level is shown in the middle area, indicating a relatively conductive phase boundary.

Supplementary Files

This is a list of supplementary files associated with this preprint. Click to download.

- Supplementaryinformation.docx
- ExtendedDataFigures.pdf